RSC Advances

PAPER

View Article Online
View Journal | View Issue



Cite this: *RSC Adv.*, 2026, **16**, 29132

# Interfacial Fe–Mo electronic coupling in $FeMoO_4$/carbon hybrids for efficient and durable alkaline overall water splitting

Rajini Murugesan,[a] Manova Santhosh Yesupatham,[a] Mandana Amiri[b] and Arthanareeswari Maruthapillai *[a]

Biomass-derived materials have emerged as sustainable and low-cost platforms for designing next-generation electrocatalysts owing to their natural abundance, tunable porosity, and carbon-rich frameworks. In this context, water splitting demands efficient electrocatalysts capable of driving both the oxygen evolution reaction (OER) and hydrogen evolution reaction (HER). Herein, we develop a biomass-oriented hybrid electrocatalyst, $FeMoO_4$@Ds-AC, by anchoring $FeMoO_4$ particles with hierarchically porous activated carbon derived from date seed waste, thereby coupling catalytic activity with sustainable material design. The $FeMoO_4$Ds-AC catalyst improves the OER performance in an alkaline medium, achieving a low overpotential of 334 mV at 20 mA $cm^{-2}$ and a Tafel slope of 84 mV $dec^{-1}$. Subsequently, it shows an effective HER activity, with an overpotential of 75 mV at 10 mA $cm^{-2}$. The catalyst splits water with a cell voltage of 1.642 V at 10 mA $cm^{-2}$. $FeMoO_4$@Ds-AC has outstanding long-term durability exceeding 100 hours for both the HER and OER, with low performance degradation. The enhanced activity is attributed to the synergistic interaction between redox-active $FeMoO_4$ and the conductive, porous carbon matrix, which accelerates charge transfer and increases active-site accessibility. Furthermore, density functional theory (DFT) calculations are performed to gain deep insights into the interfacial coupling between $FeMoO_4$ and Ds-AC. The lowest interaction distance between $FeMoO_4$ and Ds-AC confirms the strong Fe–C and Mo–C covalent bonding and large negative binding energy (−4.61 eV), representing exothermic binding. In addition, the electronic structure analysis reveals that the strong orbital hybridization between the Mo-3d, Fe-3d and C-2p states further confirms the electronic coupling bonding between the interfacial materials. Finally, the charge density difference plots reveal that the electron density redistribution between the interfaces indicates strong Fe–C and Mo–C covalent bonding. Our DFT observations clearly demonstrate that Fe–C and Mo–C coupling enhances charge transfer and influences the OER performance. This paper describes a sustainable and effective technique for developing biomass-derived bifunctional electrocatalysts for water splitting applications.

Received 6th March 2026
Accepted 8th May 2026

DOI: 10.1039/d6ra01930g

rsc.li/rsc-advances



## 1 Introduction

The growing global demand for clean and sustainable energy has put tremendous pressure on scientists to produce viable alternatives to fossil fuels. Hydrogen ($H_2$) is a promising energy carrier with high energy density and minimal carbon emissions after combustion.[1] Water electrolysis is one of the most sustainable and scalable methods for producing hydrogen using two half-reactions: the oxygen evolution reaction (OER) at the anode and the hydrogen evolution reaction (HER) at the cathode.[2] Although the general procedure appears simple, its practical implementation is hampered by low reaction rates, particularly for the OER, which involves a complex four-electron transfer pathway with significant overpotential needs.[3] At the same time, efficient HER activity is also required to achieve balanced and energy-efficient total water splitting. As a result, the development of bifunctional electrocatalysts capable of efficiently driving both the OER and HER is extremely desirable for practical water electrolysis systems. To overcome these issues, significant efforts have been made to develop highly efficient, stable, and cost-effective electrocatalysts capable of accelerating reaction kinetics and facilitating rapid charge transfer.[4] Noble metal-based catalysts, including $RuO_2$ and $IrO_2$ for the OER and Pt-based materials for the HER, are considered cutting-edge due to their high catalytic activity.[5,6] However, their exorbitant cost, limited availability, and poor long-term

[a]*Department of Chemistry, Faculty of Engineering and Technology, SRM Institute of Science and Technology, Kattankulathur, Tamil Nadu, 603203, India. E-mail: arthanam@srmist.edu.in*

[b]*Laboratory for Life Sciences and Technology (LiST), Faculty of Medicine and Dentistry, Danube Private University, Krems, 3500, Austria*

durability limit their widespread use.[7] As a result, current research has concentrated on earth-abundant transition metal-based materials, including those containing iron (Fe), cobalt (Co), nickel (Ni), and molybdenum (Mo), which have tunable electronic structures, numerous oxidation states, and advantageous redox characteristics.[8–10] Iron molybdate ($FeMoO_4$) has gained attention for its potential catalytic activity as a bimetallic oxide system.[11–13] The interaction of Fe and Mo centers is expected to affect the electronic structure and adsorption behavior of reaction intermediates, improving catalytic performance. However, the practical application of immaculate $FeMoO_4$ is restricted by its low electrical conductivity, limited surface area, and inadequate exposure of active areas.[14–16] To circumvent these limitations, combining metal oxides with conductive carbon frameworks has proven to be a viable method. Biomass-derived carbon compounds, in particular, have sparked widespread interest because to their hierarchical porosity, high electrical conductivity, and sustainability, providing a synergistic foundation for efficient overall water splitting.[17] Biomass-derived carbon materials, such as those derived from energy crops, agricultural residues, and forestry waste, have emerged as promising catalyst precursors due to their high carbon content, abundance, and low cost.[18] These materials have tunable porosity, high electrical conductivity, and structural versatility, making them ideal for developing efficient electrocatalysts. Long *et al.* developed a NiFeP/NiFe-LDH heterojunction system with efficient bifunctional activity. It required overpotentials of 341 mV for OER and 210 mV for HER and achieved overall water splitting at 1.526 V and 10 mA $cm^{-2}$.[19] Yang *et al.* found Fe and N co-doped biomass-derived carbon to be a high-performance bifunctional electrocatalyst, achieving low overpotentials of 265 mV for OER and 92 mV for HER at 10 mA $cm^{-2}$ and an overall water splitting voltage of 1.53 V.[20] Gayathri *et al.* synthesized biowaste-derived carbon (Fe@PSAC) catalyst with a cell voltage of 1.58 V at 10 mA $cm^{-2}$.[21] Similarly, the conversion of aloe wastes,[22–24] Magnolia leaf wastes,[25] ginkgo leaf wastes,[26,27] cauliflower leaf wastes,[28] neem leaves,[29] Jasminum leaves[30] and alfalfa plant wastes[31] into useable carbon supports circular economy concepts, minimizes environmental difficulties and contributes to global decarbonization efforts. These studies demonstrate the effectiveness of combining transition metal compounds and conductive frameworks to improve catalytic performance for overall water splitting.

Herein, we report a biomass-derived hybrid electrocatalyst, $FeMoO_4$Ds-AC, constructed by anchoring $FeMoO_4$ nanoparticles onto activated carbon from date seed waste. Incorporating $FeMoO_4$ into Ds-AC improves electrical conductivity and the dispersion of active sites, overcoming the inherent limitations of metal oxides. The carbon framework is porous and conductive, facilitating fast electron transport and easy access to electrolytes. $FeMoO_4$ provides redox-active centers for catalytic reactions. The $FeMoO_4$@Ds-AC catalyst improves bifunctional activity for both OER and HER, allowing for efficient water splitting under alkaline conditions. To determine the catalyst's performance, comprehensive structural, surface, and electrochemical investigations are conducted. The $FeMoO_4$@Ds-AC system exhibits improved performance compared to the individual components and demonstrates competitive activity relative to benchmark catalysts, highlighting the synergistic interaction between the metal oxide and the biomass-derived carbon matrix.

## 2 Experimental section

### 2.1 Synthesis of iron molybdate ($FeMoO_4$) nanoparticles

Iron molybdate ($FeMoO_4$) nanoparticles were synthesized through a hydrothermal method, followed by calcination. In brief, 0.1 M $FeCl_3$ and 0.2 M $Na_2MoO_4 \cdot 2H_2O$ were dissolved in 35 mL of DD water, separately. Then, the homogeneous suspension was mixed in a 250 mL beaker under constant stirring. After that, 0.5 g of urea (10 mL $H_2O$) was added to the above suspension and continuously stirred for 1 h. Then, the obtained mixture solution was transferred into a 100 mL Teflon-lined stainless-steel autoclave, heated at 180 °C for 24 h, and gradually cooled down to room temperature. The resultant products were collected by centrifugation, washed with doubly distilled water and ethanol several times to eliminate the unreacted precursor material, and dried at 60 °C overnight. Finally, the collected products were calcined at 550 °C for 4 h in an air atmosphere. The overall synthesis procedure of $FeMoO_4$ is shown in Scheme 1a.

### 2.2 Preparation of date seeds-derived activated carbon (Ds-AC)

The Ds-AC was prepared *via* a two-step process. The first step was the preparation of pre-carbonized carbon (PCC), and the second step was the chemical activation of PCC. The date seeds were washed with distilled water in order to remove dust and other inorganic impurities, dried, and further dried in an oven for 24 h at 110 °C. After the removal of all moisture content, the date seeds were carbonized at 300 °C for about 4 h under vacuum conditions and further ground well to get a fine powder. This finely ground carbon powder was labelled as Ds-derived pre-carbonized carbon (Ds-PCC). In the chemical activation process, 20 g of the Ds-derived pre-carbonized carbon powder (Ds-PCC) was mixed with 100 mL of a 3 M KOH aqueous solution. This slurry was stirred for 24 hours at room temperature to ensure thorough mixing. The prepared Ds-PCC-3 M KOH slurry was dried in an oven at 110 °C. After that, the slurry was heated up to 700 °C for 1 h in $N_2$ atmosphere at a 5 °C $min^{-1}$ heating rate. Subsequently, the resulting activated carbon was repeatedly washed with DD water until the pH of the supernatant solution was neutral. Finally, the perfectly washed activated carbon sample was dried at 110 °C for 24 h in a hot air oven, finely ground and stored in a desiccator. This prepared activated carbon sample was labelled as Ds-AC. The overall synthesis procedure of Ds-AC is shown in Scheme 1b.

### 2.3 Preparation of the $FeMoO_4$@Ds-AC nanocomposite

The $FeMoO_4$@Ds-AC nanocomposite was prepared through the sonochemical approach, wherein 5 mg of $FeMoO_4$ and 5 mg of Ds-AC were dispersed into 100 mL of DD water and ultrasonicated for 30 min. Finally, the collected products were

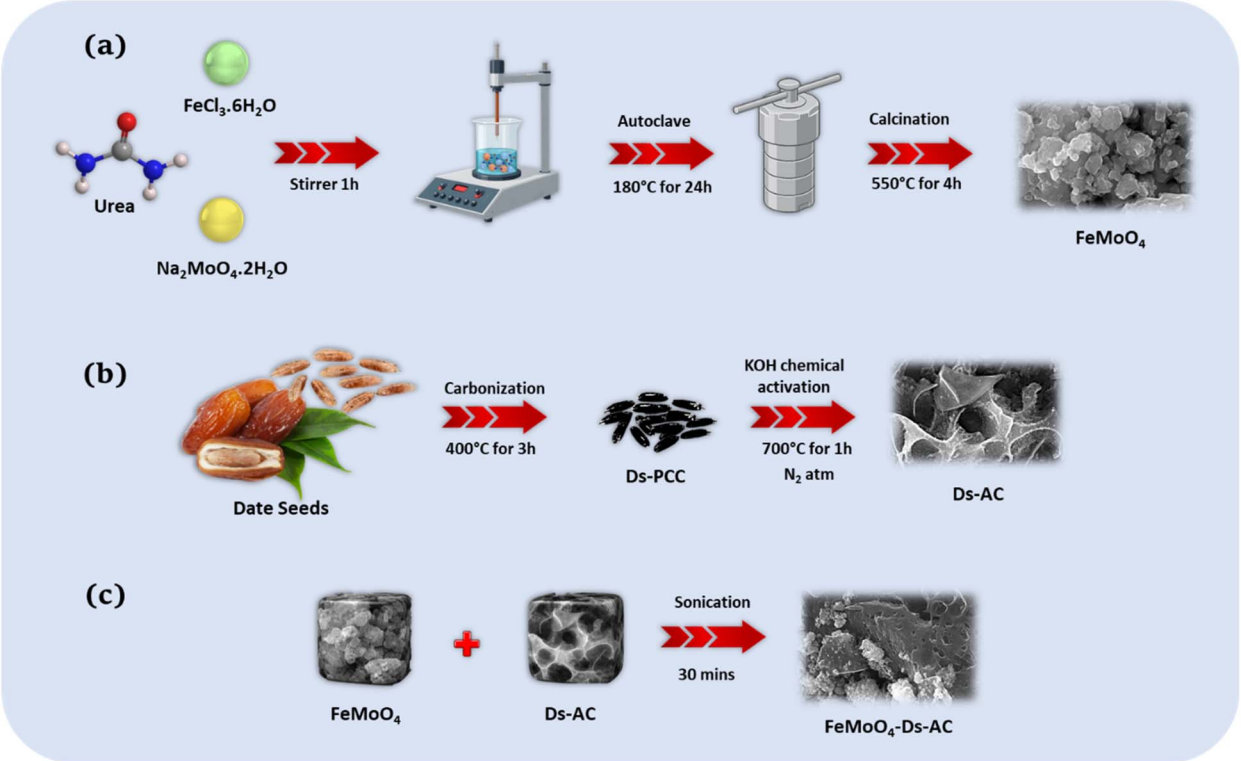


Scheme 1 (a) Illustration of the synthetic process of the $FeMoO_4$ nanocomposite. (b) Schematic of the synthesis process of Ds-AC. (c) Schematic of the synthesis process of $FeMoO_4$@Ds-AC at 60 °C overnight.

centrifuged and dried at 60 °C for 12 h, and it is denoted as $FeMoO_4$@Ds-AC nanocomposite. The overall synthesis procedure of the $FeMoO_4$@Ds-AC nanocomposite is shown in Scheme 1c.

## 3 Results and discussion

### 3.1 X-ray diffraction (XRD) analysis

The crystalline structures of the produced materials were analysed using powder XRD. The naturally occurring Ds-AC observed two broad diffraction humps at $2\theta = 24.4°$ and 43.6°, which corresponded to the (002) and (101) planes of disordered graphitic carbon, respectively (Fig. 1a).[32,33] These broad peaks suggested that Ds-AC was largely amorphous and had a low graphitization degree, which was beneficial for electrocatalysis due to the abundance of defect sites and a relatively large surface area. The structural analysis of $FeMoO_4$ showed strong diffraction peaks (Fig. 1b), indicating a well-crystallized monoclinic phase. The diffraction peaks at $2\theta$ values for the (110), (021), (220), (002), (112), (202), (222) and (440) planes are consistent with standard JCPDS no. (01-089-2367), confirming the formation of phase-pure monoclinic $FeMoO_4$. The absence of impurity-related peaks confirmed the successful synthesis of phase-pure iron molybdate. The XRD pattern of the $FeMoO_4$@Ds-AC nanocomposite (Fig. 1c) showed the unique diffraction peaks of $FeMoO_4$ and the broad carbon humps (highlighted inside of Fig. 1c) associated with Ds-AC, showing the effective integration of $FeMoO_4$ nanoparticles

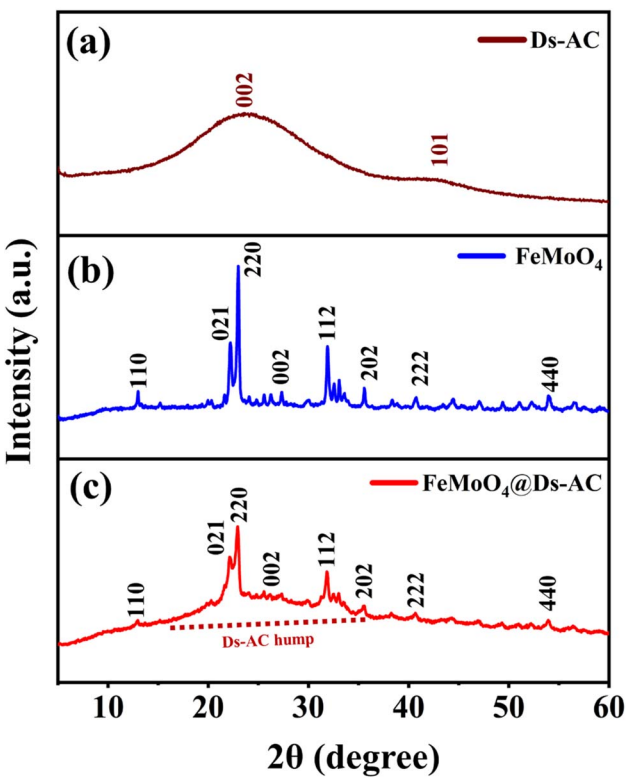


Fig. 1 XRD patterns of (a) Ds-AC, (b) $FeMoO_4$ and (c) $FeMoO_4$@Ds-AC.

inside the carbon framework. The retention of $FeMoO_4$ reflections showed that the crystalline structure of the metal oxide was preserved during the nanocomposite formation, while broad carbon characteristics indicated that the amorphous nature of Ds-AC remained unchanged. This coexistence of diffraction evidence demonstrated that hybridization occurred without the structural degradation of either component. This heterostructure was expected to improve electron transport efficiency, electrolyte accessibility and overall electrocatalytic performance during alkaline OER.

### 3.2 X-ray photoelectron spectroscopic (XPS) studies

X-ray photoelectron spectroscopy (XPS) was used to investigate the surface chemical composition and oxidation states of the $FeMoO_4$ electrocatalyst. The survey spectrum (Fig. S1a) showed the presence of Fe, Mo, and O, confirming the successful synthesis of the $FeMoO_4$ phase and its effective integration with the biomass-derived carbon support. The strong C 1s signal resulted from the Ds-AC matrix, whereas the distinct Fe 2p and Mo 3d peaks confirmed the presence of both metal species with no detectable impurities, confirming the composite's chemical purity.[12] The high-resolution Fe 2p spectrum (Fig. S1b) showed two prominent spin–orbit components centered at roughly 711.27–713.70 eV and 725.21–728.20 eV, which corresponded to Fe $2p_{3/2}$ and Fe $2p_{1/2}$, respectively, along with distinctive satellite features. Peak deconvolution demonstrated the coexistence of $Fe^{2+}$ and $Fe^{3+}$ species, with fitted components located at low and high binding energies within the Fe $2p_{3/2}$ region. The presence of significant shifts in satellite peaks confirmed the high-spin $Fe^{3+}$ configuration, which was a characteristic of iron molybdate-based oxide systems. The observed $Fe^{2+}/Fe^{3+}$ mixed-valence state occurred because of the strong Fe–O–Mo electronic interaction inside the $FeMoO_4$ lattice. This led to charge redistribution and partial electron delocalization between the Fe and Mo centers. These mixed-valence Fe redox pairs were extremely advantageous to the oxygen evolution reaction because they allow for quick electron transfer and dynamic redox cycling during anodic polarization. This electronic flexibility, together with strong metal–oxygen coordination, improved the adaptability of Fe active sites during alkaline OER operation, leading to the increased electrocatalytic activity of the $FeMoO_4$ catalyst.[34] The Mo 3d spectrum (Fig. S1c) showed two distinct peaks at 232.25 eV and 235.38 eV, corresponding to the Mo $3d_{5/2}$ and Mo $3d_{3/2}$ spin–orbit components, respectively. These binding energy positions were exclusive to the $Mo^{6+}$ species in molybdate-based compounds. There were no additional peaks corresponding to reduced Mo species ($Mo^{5+}$ or $Mo^{4+}$), demonstrating that molybdenum predominantly existed in its fully oxidized state. The presence of stable $Mo^{6+}$ centers was likely to influence the electronic environment of nearby Fe sites through Fe–O–Mo interactions, promoting charge redistribution and leading to increased electrocatalytic reaction kinetics, as previously reported for comparable Fe–Mo oxide systems.[35,36] The O 1s spectrum (Fig. S1d) showed different contributions from metal–oxygen bonds (M–O, 530.10 eV), metal–hydroxyl species (M–OH, 530.53 eV), and surface oxygenated species (C–O, 531.47 eV). The coexistence of C–O species in the C 1s spectrum and M–O components in the O 1s spectrum indicated the formation of interfacial carbon–oxygen–metal (C–O–M) connections, which allowed for effective electronic coupling and charge transfer across the carbon-oxide

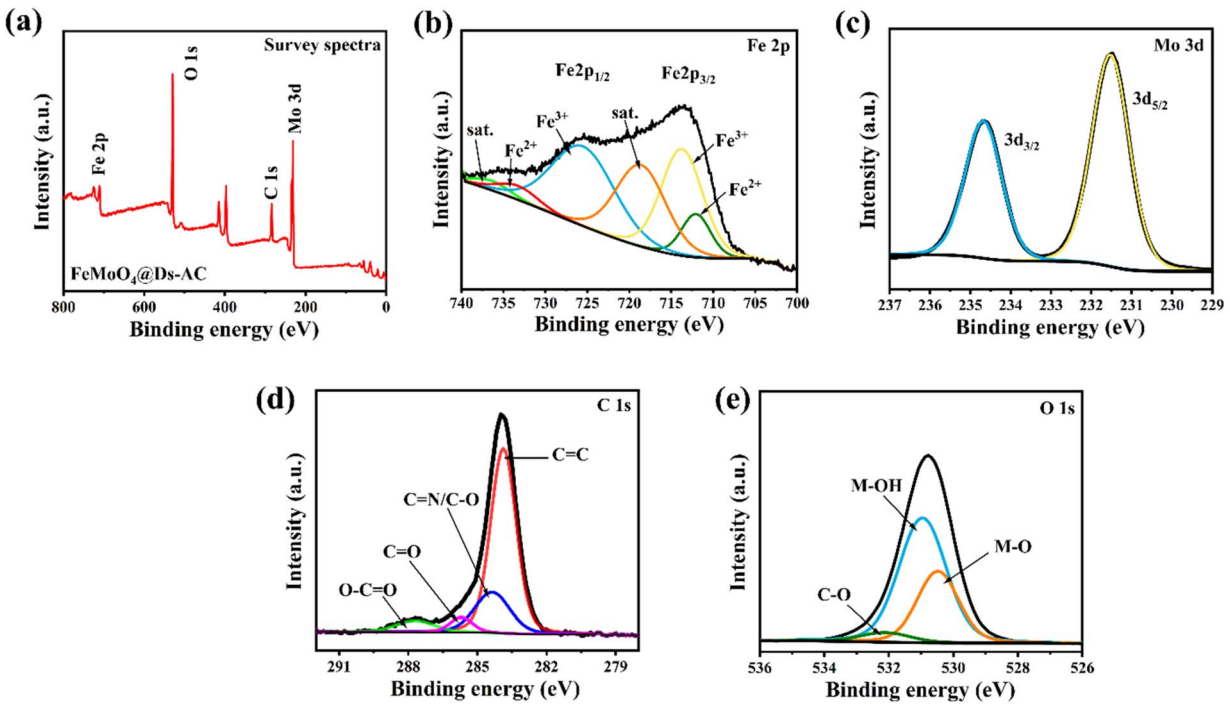


Fig. 2 (a) XPS survey spectrum of $FeMoO_4$@Ds-AC and its deconvoluted XPS sub-spectra of the (b) Fe 2p, (c) Mo 3d, (d) C 1s, and (e) O 1s orbitals.

interface.[12] The survey spectrum (Fig. 2a) of the $FeMoO_4$@Ds-AC composite showed the presence of Fe, Mo, and O, as well as an important C 1s peak, indicating the successful incorporation of biomass-derived carbon matrix. The high-resolution Fe 2p spectrum (Fig. 2b) revealed $Fe^{2+}$ and $Fe^{3+}$ species with peaks at 712.02 eV and 713.73 eV, respectively, along with distinct satellite features. Compared to pristine $FeMoO_4$, these peaks showed a positive shift of ~0.75 eV ($Fe^{2+}$) and ~0.03 eV ($Fe^{3+}$), indicating a modified electronic environment around Fe centers. The presence of $Fe^{2+}/Fe^{3+}$ redox pairs was beneficial for electrocatalysis as it promoted efficient electron transfer and dynamic redox behaviour. The Mo 3d spectrum (Fig. 2c) showed the characteristic $Mo^{6+}$ peaks, indicating the structural stability of the molybdate phase. An increase in peak intensity, especially for the Mo $3d_{3/2}$ component, indicated the improved exposure of Mo active sites in the composite. The presence of stable $Mo^{6+}$ species could affect the electronic structure of nearby Fe sites *via* Fe–O–Mo interactions. The C 1s spectrum (Fig. 2d) was divided into graphitic carbon (C=C), C–O, and O–C=O components, indicating the presence of oxygen-containing functional groups on the Ds-AC surface. These functionalities improved interfacial contact and may promote the formation of C–O–M (M = Fe and Mo) linkages, allowing for efficient charge transfer across the carbon–oxide interface. The O 1s spectrum (Fig. 2e) showed metal–oxygen (M–O) and metal–hydroxyl (M–OH) peaks at 530.43 and 530.94 eV, respectively. Compared to pristine $FeMoO_4$, these peaks showed positive shifts of ~0.33 eV (M–O) and ~0.41 eV (M–OH), indicating electron density redistribution at the interface. The presence of abundant surface hydroxyl species is especially advantageous because they are recognized as key intermediates in electrocatalytic reactions.

### 3.3 Morphological analysis

FE-SEM was used to analyse the surface morphology and structural changes of Ds-AC, $FeMoO_4$ and the $FeMoO_4$@Ds-AC nanocomposite upon hybridization. As shown in Fig. S2a–c, the Ds-AC sample formed a highly porous, foam-like shape with curved, layered textures and huge pores. This structure is typical of activated carbon generated from biomass precursors, such as date seeds, and it increases mass transport and increases electrochemical surface area. Fig. S3a–c shows the morphology of the $FeMoO_4$ particles, made up of asymmetrical small particles clustered tightly together, providing a dense and rough surface. These particles were closely packed, resulting in a compact structure but with a low accessible surface area due to particle aggregation. The SEM picture of the $FeMoO_4$@Ds-AC nanocomposite (Fig. 3a–c) showed a well-integrated hybrid structure, with the $FeMoO_4$ particles uniformly linked to the porous carbon surface. Ds-AC's foam-like carbon structure provided structural support and uniformly dispersed $FeMoO_4$ to prevent agglomeration. The close interactions between $FeMoO_4$ and Ds-AC improved smooth electron transport, charge transfer performance and the number of exposed active sites, all of which led to improved electrocatalytic activity. Furthermore, SEM-EDS elemental mapping, as shown in Fig. S2d–f, S3d–g

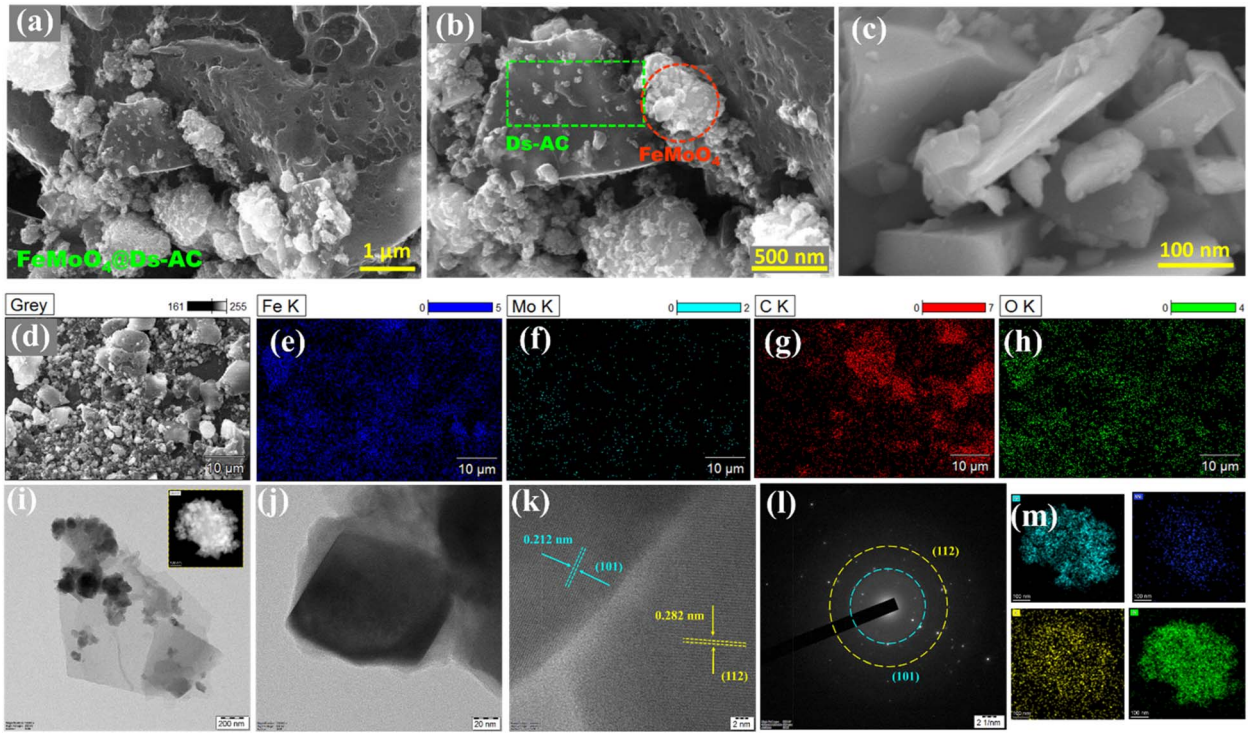


Fig. 3 (a–c) FE-SEM images of $FeMoO_4$@Ds-AC. (d) SEM image of $FeMoO_4$@Ds-AC. (e–h) EDS elemental mapping images of $FeMoO_4$@Ds-AC. (i and j) HR-TEM micrographs of $FeMoO_4$@Ds-AC. (k) Lattice fringes of $FeMoO_4$@Ds-AC. (l) SAED pattern of $FeMoO_4$@Ds-AC. (m) Corresponding HR-TEM elemental mapping images of Fe, Mo, C, and O.

and 3d–h, confirmed the uniform distribution of the elements C and O in Ds-AC; Fe, Mo, and O in $FeMoO_4$; and Fe, Mo, C, and O in $FeMoO_4$@Ds-AC, throughout the nanocomposite, showing excellent synthesis and material hybridization. Also, the ED table and ED spectrum of Ds-AC, $FeMoO_4$ and $FeMoO_4$@Ds-AC are displayed in Fig. S4, S5 and S6, respectively. The $FeMoO_4$@Ds-AC nanocomposite's crystalline structure and crystallinity were studied using HRTEM and selected area electron diffraction (SAED). The HRTEM image (Fig. 3i and j) showed that the $FeMoO_4$ nanoparticles were strongly attached to a transparent sheet-like carbon matrix (Ds-AC), indicating high active-phase dispersion. The interface between $FeMoO_4$ and Ds-AC was confirmed by visible lattice fringes, with interplanar spacings of 0.282 nm and 0.212 nm, corresponding to the (112) plane of $FeMoO_4$ and the (101) plane of Ds-AC (Fig. 3k and l). The respective mappings of all the current elements to images and colors are given in Fig. 3m. These characteristics validated the crystalline nature of both components and confirmed the successful nanocomposite of $FeMoO_4$ and the (101) plane of Ds-AC, which matched well with the XRD results and further confirmed the structural integrity and phase composition of the hybrid material.

Furthermore, these findings were well aligned with the structural characteristics revealed by XRD and HR-TEM analyses. The superior overall water splitting performance of the $FeMoO_4$@Ds-AC nanocomposite can be attributed to the strong synergistic electronic interaction between $FeMoO_4$ and the defect-rich Ds-AC support. This interaction effectively modulated the adsorption energetics of the key intermediates, facilitating optimized hydrogen adsorption/desorption (*H) at the cathodic sites for HER, alongside the favorable adsorption and transformation of oxygenated intermediates (*OH, *O, and *OOH) at the anodic sites for OER. The intimate interfacial coupling between $FeMoO_4$ nanoparticles and the conductive carbon matrix induced electronic redistribution around the Fe active centers, thereby enhancing local charge density and redox flexibility. This was further confirmed by XPS analysis, where the O 1s spectrum revealed the presence of abundant defect-related oxygen species and adsorbed oxygen components, indicating a high density of surface defects and oxygen vacancies, which were beneficial for intermediate adsorption and activation, particularly during alkaline OER. In addition, the significantly higher double-layer capacitance ($C_{dl}$) of $FeMoO_4$@Ds-AC suggested an increased number of electrochemically accessible active sites. These defect sites, along with interfacial Fe–O–C linkages, were expected to lower the energy barrier for *OOH formation, which was widely recognized as the rate-determining step in alkaline OER. Simultaneously, the conductive Ds-AC framework provided efficient electron transport pathways, as evidenced by the reduced charge-transfer resistance observed in EIS measurements, thereby ensuring rapid electron delivery to active sites and promoting efficient HER kinetics. Collectively, these structural and electronic advantages accelerate both hydrogen evolution and the four-electron oxygen evolution pathways, resulting in enhanced bifunctional catalytic activity and long-term durability. Based on these insights, the synergistic HER and OER mechanism of the $FeMoO_4$@Ds-AC catalyst is schematically illustrated in Scheme 2.

# 4 Electrochemical performance

## 4.1 Electrocatalytic OER performance

For identifying the actual potential of the $FeMoO_4$@Ds-AC catalyst for TWS, we conducted a systematic electrochemical evaluation with 1.0 M KOH as the electrolyte, $FeMoO_4$@Ds-AC as the working electrode (coated on NF), and Hg/HgO as the reference electrode. A platinum rod and bare NF were used as

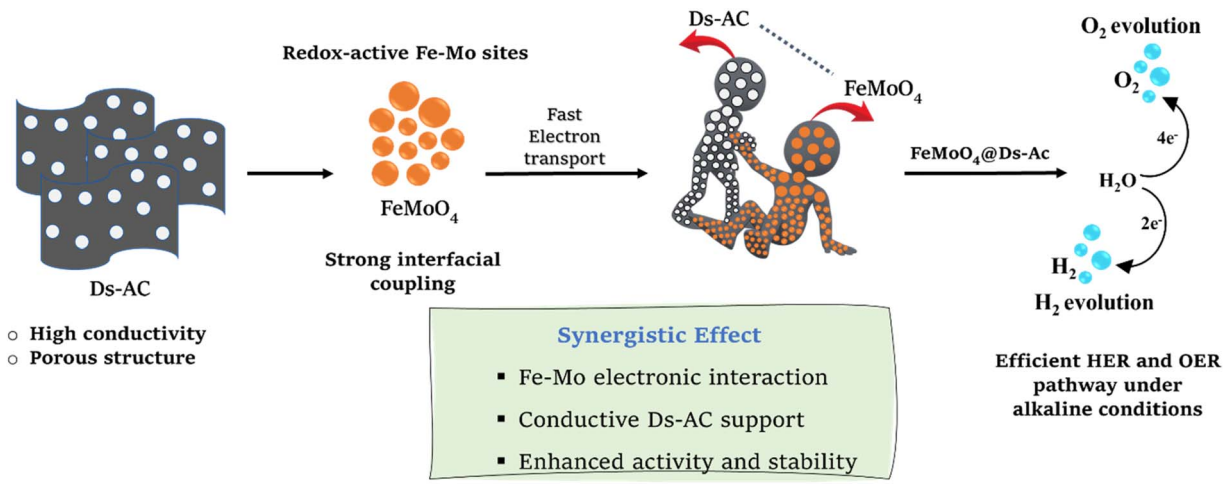


Scheme 2 Schematic of the synergistic overall water splitting (HER and OER) mechanism over the $FeMoO_4$@Ds-AC catalyst. The conductive and porous biomass-derived Ds-AC support facilitates rapid electron transport and the uniform dispersion of the $FeMoO_4$ nanoparticles, while the redox-active Fe–Mo sites promote efficient water dissociation and optimized hydrogen adsorption/desorption (*H) for the HER at the cathode, along with the favorable adsorption and conversion of the OER intermediates (*OH, *O and *OOH) at the anode. The combined Fe–Mo electronic interactions and carbon coupling lead to the enhanced bifunctional catalytic activity and long-term stability in alkaline media.

the counter electrodes for OER and HER, respectively. The main plot started with the most direct measure of catalytic performance by linear sweep voltammetry (LSV), which assessed the overpotential mandatory to generate OER at a given current density (Table S1). A low overpotential not only signified small energy input but also high intrinsic catalytic activity. Among all tested samples (Fig. 4a), $FeMoO_4$@Ds-AC stood out because it needed only 334 mV to reach 20 mA $cm^{-2}$, which was lower than those required by pristine $FeMoO_4$ (341 mV), Ds-AC (398 mV), and bare NF (549 mV) and was comparable to that required by the commercial $RuO_2$ (307 mV) catalyst. This remarkable improvement was due to the synergistic interaction of redox-active $FeMoO_4$ and a highly conductive, porous carbon nanocomposite generated from date seeds. The carbon support not only prevented $FeMoO_4$ nanoparticle agglomeration, but it also improved interaction with the electrolyte, increasing electron and ion transport. However, activity alone is insufficient; we must also remember to take a look at reaction kinetics, which we achieved *via* Tafel analysis. The Tafel slope provides an understanding of the reaction pathway and rate-determining steps of OER. A smaller slope denotes faster kinetics and better kinetics for intermediate production and degradation. $FeMoO_4$@Ds-AC had the lowest Tafel slope of 84 mV $dec^{-1}$, defeating Ds-AC (123 mV $dec^{-1}$), $FeMoO_4$ (128 mV $dec^{-1}$), and NF (190 mV $dec^{-1}$), but not the benchmark catalyst $RuO_2$ (67 mV $dec^{-1}$) (Fig. 4b). This demonstrated the catalyst's ability to facilitate fast electron transport and intermediate conversion steps. The presence of $Fe^{2+}/Fe^{3+}$ and $Mo^{6+}/Mo^{5+}$ redox couples contributed to dynamic active site reconfiguration under applied potential, improving reaction kinetics. Furthermore, electronic manipulation by the carbon matrix enhanced the adsorption energy of important OER intermediates (*OH, *O, and *OOH), permitting high turnover rates. To get a deep understanding of the charge transport behaviour at the electrode–electrolyte interface, we carried out electrochemical impedance spectroscopy (EIS). The technique exposes the charge transfer resistance ($R_{ct}$), a significant parameter that indicates how efficiently electrons move along the interface.

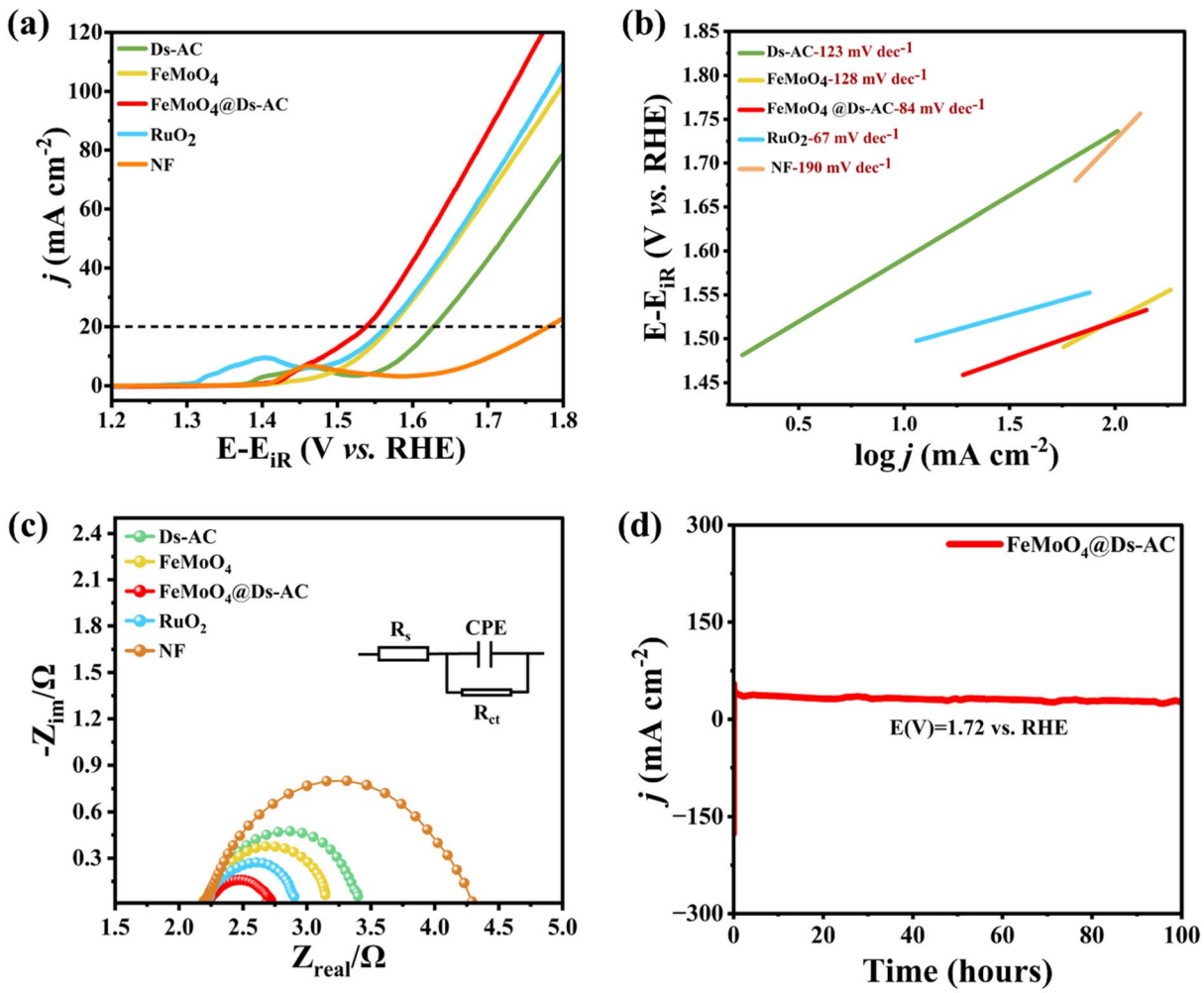


Fig. 4 (a) iR-corrected OER linear sweep voltammograms of Ds-AC, $FeMoO_4$, $FeMoO_4$@Ds-AC, and NF in comparison with that of the commercial $RuO_2$ catalyst. (b) Tafel analyses of Ds-AC, $FeMoO_4$, $FeMoO_4$@Ds-AC, and NF in comparison with that of the commercial $RuO_2$ catalyst plotted from SCV curves. (c) Corresponding Nyquist plots for Ds-AC, $FeMoO_4$, $FeMoO_4$@Ds-A, NF, and $RuO_2$ catalysts (inset shows the equivalent circuit used for fitting the EIS data). (d) Stability graph of $FeMoO_4$@Ds-AC over 100 hours.

Due to its metallic nature, $RuO_2$ exhibited the lowest $R_{ct}$ (0.480 Ω), while $FeMoO_4$@Ds-AC had a considerably lower $R_{ct}$ of 0.708 Ω, and this was clearly better than those of $FeMoO_4$ (0.953 Ω), Ds-AC (1.211 Ω) and NF (2.095 Ω). This ideal resistance balance showed that the combination catalyst offered good electrical conductivity without lowering the number of active sites (Fig. 4c). The carbon network and $FeMoO_4$ were interconnected, resulting in the formation of rapid electron highways and the reduction of recombination losses. Such favourable interfacial characteristics were crucial for maintaining high OER rates over a long period. Understanding the number of active sites available for catalysis is also extremely important; therefore, we calculated the electrochemically active surface area (ECSA) using double-layer capacitance ($C_{dl}$) measurements presented in Fig. S4. A higher $C_{dl}$ value usually indicates more exposed active sites and greater surface availability. $FeMoO_4$@Ds-AC had the highest $C_{dl}$ of 77.62 mF $cm^{-2}$, defeating $FeMoO_4$ (60.62 mF $cm^{-2}$), Ds-AC (21 mF $cm^{-2}$) and NF (26.87 mF $cm^{-2}$). This noticeable rise was due to the porous nature of the carbon support, which facilitated electrolyte infiltration and maximized catalyst utilization (Fig. S8a). The significant number of accessible sites was most probably due to the uniform dispersion of $FeMoO_4$ nanoparticles across the high-surface-area carbon framework, which allowed a large portion of the catalyst to actively participate in the reaction. Furthermore, the most superior $FeMoO_4$@Ds-AC nanocomposite demonstrated outstanding stability over 100 hours (Fig. 4d). The $FeMoO_4$@Ds-AC catalyst was highly durable due to the strong interfacial connection between the $FeMoO_4$ nanoparticles and the defect-rich Ds-AC framework. This avoided nanoparticle agglomeration and reduced Fe/Mo dissolution under strongly alkaline OER conditions. Furthermore, the hierarchically porous and structurally robust carbon structure allowed for excellent electrical contact and continued electrolyte penetration during extended polarization, preserving structural integrity, active site accessibility, and long-term catalytic activity. The bar plot presented in Fig. S8b indicates how $FeMoO_4$@Ds-AC is superior to other catalysts as a result of OER activity. The respective bar plots of overpotential and Tafel slope values compared our prepared catalysts with the benchmark

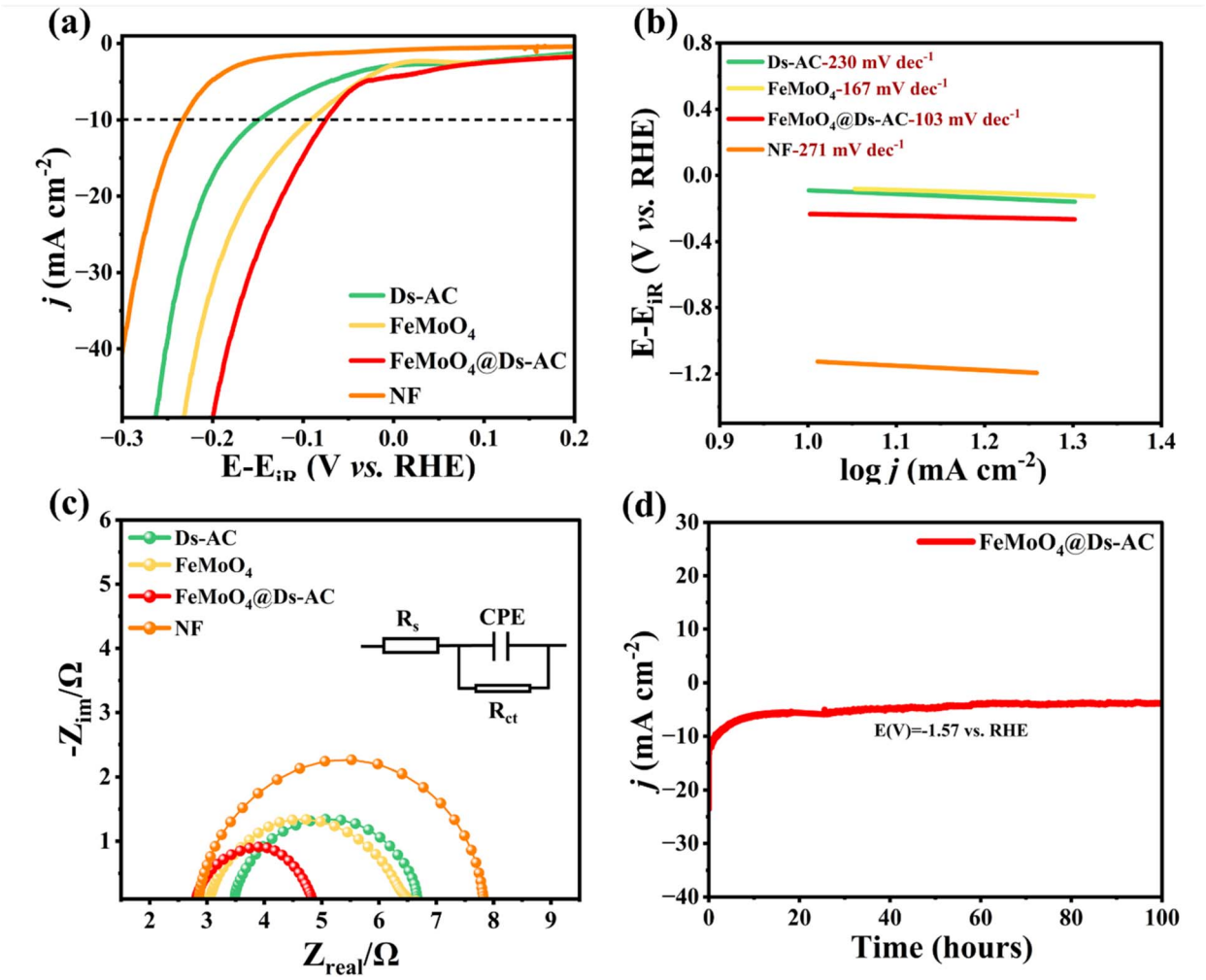


Fig. 5 (a) iR-corrected HER linear sweep voltammograms of the Ds-AC, $FeMoO_4$, $FeMoO_4$@Ds-AC, and NF catalysts. (b) Tafel analyses of the Ds-AC, $FeMoO_4$, $FeMoO_4$@Ds-AC, and NF catalysts plotted from SCV curves. (c) Corresponding Nyquist plots for the Ds-AC, $FeMoO_4$, $FeMoO_4$@Ds-AC, and NF catalysts (inset shows the equivalent circuit used for fitting the EIS data). (d) Stability graph of $FeMoO_4$@Ds-AC over 100 hours.

catalyst. $FeMoO_4$@Ds-AC exhibited enhanced performance compared to the other samples, owing to its improved intrinsic activity, accelerated reaction kinetics, reduced charge transfer resistance, and increased active surface area, collectively contributing to its efficient OER activity. The dual functioning of $FeMoO_4$ (as a redox-active core) and Ds-AC (as a conductive, porous scaffold) resulted in a tightly interconnected electrocatalytic system. The close contact between these components confirmed excellent interaction, allowing them to maximize their potential in accelerating the sluggish four-electron OER process under alkaline conditions.

### 4.2 Electrocatalytic HER performance

The HER activity of the prepared electrodes was measured with LSV curves (Fig. 5a). The $FeMoO_4$@Ds-AC catalyst delivered 10 mA $cm^{-2}$ at 75 mV, which was lower than those of $FeMoO_4$ (91 mV), Ds-AC (149 mV), and NF (233 mV), indicating superior catalytic efficiency. The incorporation of $FeMoO_4$ with the conductive Ds-AC matrix improved performance by enabling effective electron transport and the better utilization of active sites. Tafel plots were used to further analyze the reaction kinetics (Fig. 5b). $FeMoO_4$@Ds-AC had a Tafel slope of 103 mV $dec^{-1}$, which was significantly lower than those of $FeMoO_4$ (167 mV $dec^{-1}$), Ds-AC (230 mV $dec^{-1}$), and NF (271 mV $dec^{-1}$). This value indicated that the HER followed a Volmer–Heyrovsky pathway, with the electrochemical desorption step playing a dominant role. The lower slope indicated that proton adsorption and hydrogen evolution were more efficient on the composite surface. Charge transfer behaviour was investigated using EIS measurements (Fig. 5c). The $FeMoO_4$@Ds-AC electrode had the lowest charge transfer resistance ($R_{ct}$ = 2.01 Ω), which was significantly lower than those of $FeMoO_4$ (3.45 Ω), Ds-AC (3.18 Ω), and NF (4.97 Ω). This low resistance suggested fast interfacial electron transfer kinetics. The interconnected carbon framework improved conductivity by providing efficient electron pathways and maintaining intimate contact with $FeMoO_4$ active sites. Long-term chronoamperometric measurements were used to assess the catalyst's durability (Fig. 5d). The $FeMoO_4$@Ds-AC electrode maintained a stable

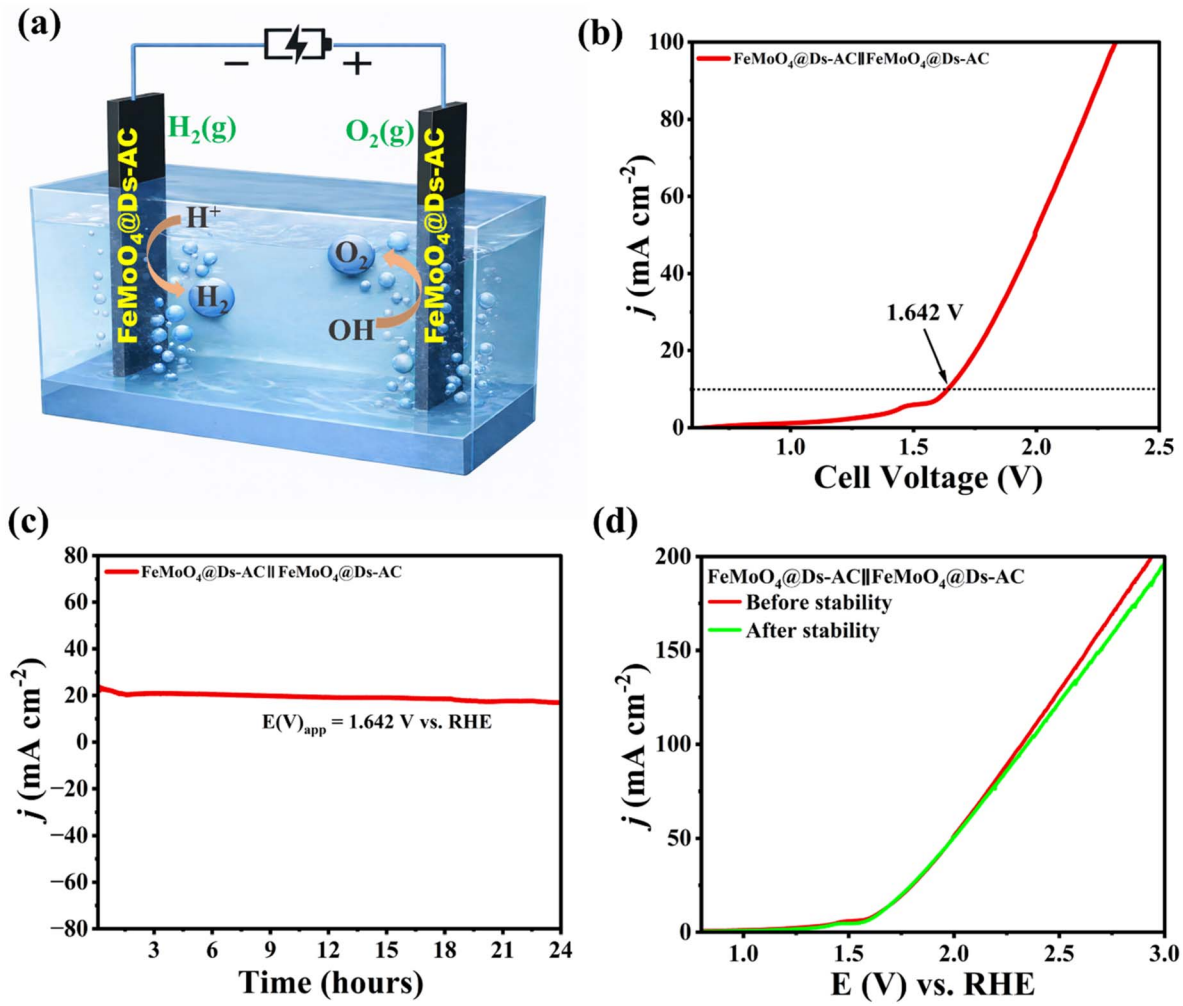


Fig. 6 (a) Schematic representation for two-electrode alkaline water splitting system using $FeMoO_4$@Ds-AC. (b) LSV polarization graph for total water splitting with $FeMoO_4$@Ds-AC used both as anode and cathode. (c) Stability study of the $FeMoO_4$@Ds-AC-based cell at 1.642 V for 24 hours. (d) LSV polarization graph before and after the stability test of the $FeMoO_4$@Ds-AC//$FeMoO_4$@Ds-AC electrode.

current density over 100 hours with minimal degradation, demonstrating its exceptional operational stability. Finally, the bar plot presented in Fig. S9 shows how $FeMoO_4$@Ds-AC is superior to other catalysts as a result of HER activity. The robust performance was primarily due to the strong interaction between $FeMoO_4$ and the carbon framework, which maintained structural integrity during continuous operation. The $FeMoO_4$@Ds-AC composite enhanced HER activity through improved charge transfer kinetics and stable active sites, making it an efficient hydrogen evolution electrocatalyst in alkaline media. In Table S2, a comparison of overpotential values with those reported for other biomass-carbon-based HER and OER electrocatalysts is provided. These characterizations combine to tell a fascinating story about material design and performance.

### 4.3 Total water splitting performance

$FeMoO_4$@Ds-AC demonstrated exceptional half-cell performance, prompting further evaluation in a two-electrode configuration for water splitting. A two-electrode setup was employed using $FeMoO_4$@Ds-AC as both anode and cathode in a 1 M KOH electrolyte. The evolution of gas bubbles on both electrodes, as illustrated in the inset of Fig. 6a, indicates that OER and HER occur simultaneously. The $FeMoO_4$@Ds-AC‖$FeMoO_4$@Ds-AC system achieved a current density of 10 mA $cm^{-2}$ at a low cell voltage of 1.642 V, as seen in Fig. 6b. In addition, long-term durability was assessed using chronoamperometric measures at room temperature. Fig. 6c shows that the $FeMoO_4$@Ds-AC electrolyzer remained stable for 24 hours at a current density of 10 mA $cm^{-2}$. The polarization curves of the $FeMoO_4$@Ds-AC//$FeMoO_4$@Ds-AC full-cell were recorded before and after long-term stability testing, demonstrating minimal performance degradation and excellent durability under alkaline water splitting conditions.

## 5 Post stability studies

In order to further investigate the morphology and structural evolution of $FeMoO_4$@Ds-AC after the OER reaction, SEM and XRD analyses were carried out following a 24 h stability test on a nickel foam. The XRD pattern of $FeMoO_4$@Ds-AC after the stability test (Fig. S10a) further confirmed the structural integrity of the composite. The characteristic diffraction peaks corresponding to crystalline $FeMoO_4$ were retained after 24 h of operation, indicating that the primary phase remained stable during OER. A broad hump observed in the $2\theta$ range of ~15–30° was attributed to the amorphous Ds-AC carbon framework. No significant peak shift or emergence of additional impurity phases was detected, demonstrating that the catalyst underwent minimal structural degradation. As shown in Fig. S10b–d, the nanocomposite architecture of $FeMoO_4$@Ds-AC remains largely preserved after prolonged OER operation, indicating good structural robustness under alkaline electrochemical conditions. The $FeMoO_4$ particles were still uniformly distributed over the Ds-AC matrix, although slight surface agglomeration could be observed, which may have resulted from prolonged electrochemical polarization and partial surface reconstruction during OER. At high magnification, the intimate contact between the $FeMoO_4$ nanoparticles and the carbonaceous substrate was maintained, suggesting strong interfacial adhesion that contributed to the stability of the catalyst. Also, the elemental distribution spectra shown in Fig. S12a and b confirm that the $FeMoO_4$@Ds-AC catalyst remains stable even when faced with strong anodic potential for a long time. Overall, the combined SEM and XRD results confirmed the excellent morphological and phase stability of $FeMoO_4$@Ds-AC during long-term OER testing.

## 6 Computational details

Density functional theory computations were used to probe the bonding and coupling between the Fe and Mo atoms in the $FeMoO_4$ material and the carbon atom of the Ds-AC sheet. First, the bonding behavior between the hybrid materials could be analyzed using the minimum energy geometry of the material. Thus, we optimized the $FeMoO_4$@Ds-AC hybrid catalyst to identify the minimum energy geometry. The optimized structure of the $FeMoO_4$@Ds-AC hybrid catalyst is provided in Fig. 7a and b (side and top views). It shows that $FeMoO_4$ is strongly anchored/stabilized onto the Ds-AC sheet through multiple interfacial bonding, including Fe–C, Mo–C, and O–C interactions. The equilibrium distances of Fe–C and Mo–C were approximately 2.07 Å and 2.30 Å, which inferred the formation of stable chemisorptive bonding rather than weak van der Waals interactions. The $FeMoO_4$ structure underwent slight distortion upon interaction with the Ds-AC monolayer, suggesting significant interfacial electronic interaction. This structural deformation facilitated enhanced orbital overlap between the Fe, Mo, and O atoms and the Ds-AC support. Such strong anchoring ensured structural stability and tuned the electronic property of the interfacial material. To quantitatively evaluate the interaction strength of $FeMoO_4$ on the Ds-AC sheet, the binding energy ($E_{bin}$) was calculated using the following equation:

$$E_{bin} = E_{FeMoO_4+Ds\text{-}AC} - (E_{FeMoO_4} + E_{Ds\text{-}AC}),$$

where $E_{FeMoO_4+Ds\text{-}AC}$ is the total energy of the optimized $FeMoO_4$@Ds-AC interface, $E_{FeMoO_4}$ is the energy of bare $FeMoO_4$, and $E_{Gra}$ is the energy of the Ds-AC sheet. The calculated binding energy of $FeMoO_4$ at the Ds-AC support was −4.61 eV, indicating an exothermic binding, *i.e.*, energetically stable and more favourable binding of $FeMoO_4$ with the Ds-AC support. The large negative value confirmed that the hybrid formation was thermodynamically more stable and easier to synthesize under standard experimental conditions. Also, it was interesting to note that this strong binding interaction suggested the formation of robust Fe–C and Mo–C interfacial bonds, which facilitated efficient electronic coupling at the $FeMoO_4$/carbon interface. This was consistent with the observed structural distortion and shortened interfacial bond distances. Consequently, the significant binding strength played a crucial role in stabilizing the hybrid structure and

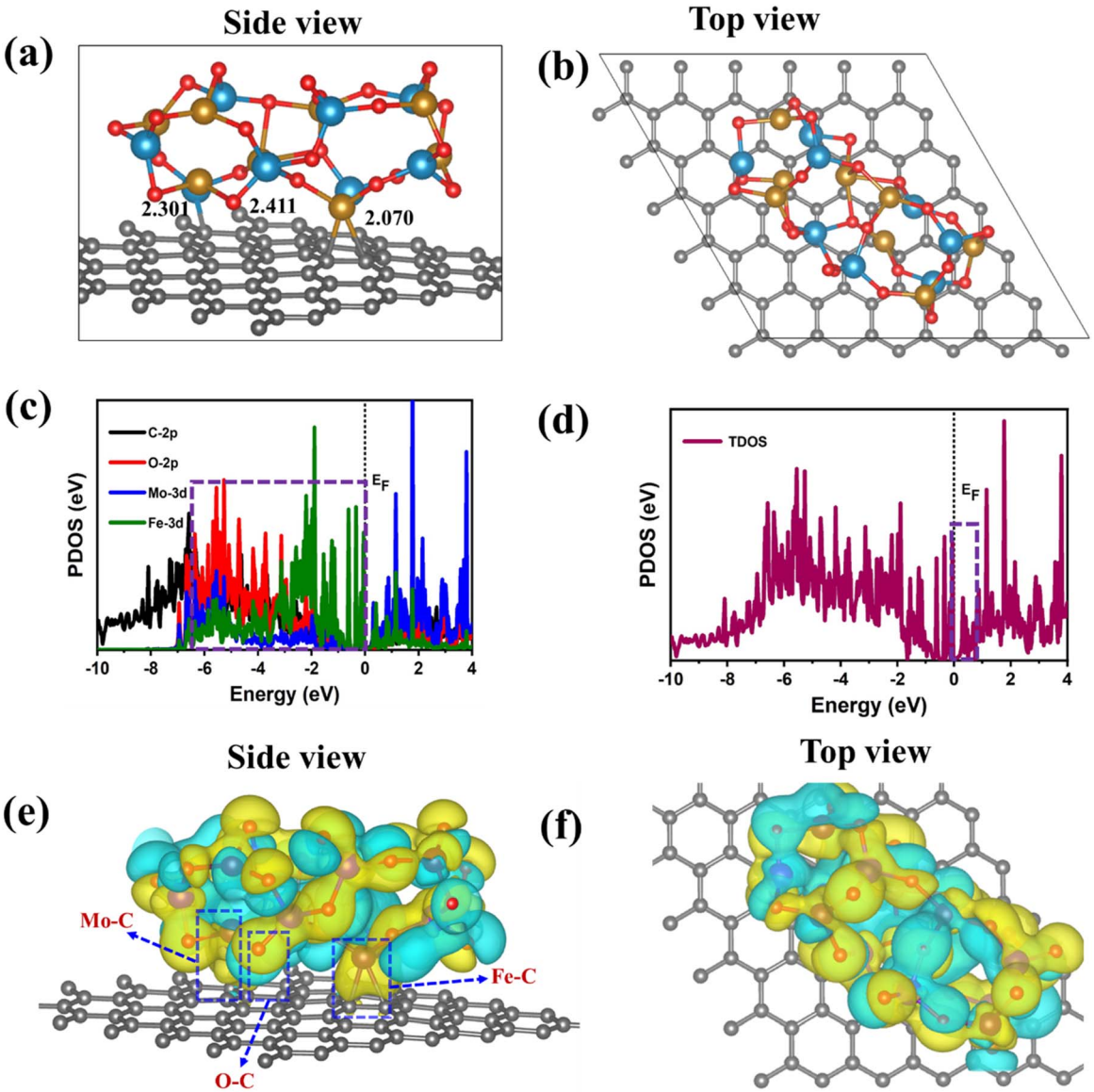


Fig. 7 Optimized geometries of the (a) side and (b) top views of the $FeMoO_4$@Ds-AC interface. The distance between $FeMoO_4$ and Ds-AC was given in Å. (c) Projected density of states and (d) total density of states plots of the $FeMoO_4$@Ds-AC interface. (e and f) Electron density difference plots of the $FeMoO_4$@Ds-AC interface. Yellow represents the charge accumulation. The isosurface value is set as 0.02 e per Bohr.[3]

modulating its electronic properties, which was beneficial for enhanced OER activity.

To further elucidate the nature of the interfacial interaction, the projected density of states (PDOS) was performed (Fig. 7c). The PDOS revealed a significant contribution of Fe-3d, Mo-3d, O-2p, and C-2p states in the valence band region (VB), indicating the strong electronic hybridization of $FeMoO_4$ with the Ds-AC support. In particular, the Fe-3d and Mo-3d orbitals exhibited noticeable overlap with O-2p states from −2.2 eV to −6.4 eV of the VB, suggesting metal–oxygen covalent interactions within the $FeMoO_4$ catalyst. It was important to note that the overlap of the C-2p states with the Fe-3d and Mo-3d orbitals in the same energy region indicated the Mo–C and Fe–C coupling between the $FeMoO_4$ and Ds-AC monolayers. Furthermore, the increased density of states near the Fermi level ($E_f$) in the TDOS (refer to Fig. 7d) indicated the enhanced electrical conductivity of the hybrid system. This electronic enhancement was crucial for facilitating rapid charge transfer during the OER. Notably, the simultaneous overlap of the Fe-3d and Mo-3d states suggested a redistribution of electronic states between the Fe and Mo atoms. This behavior was indicative of Fe–Mo electronic coupling, where the d-orbitals of Fe and Mo interacted through bridging oxygen atoms and the conductive carbon support.

To further closely visualize the $FeMoO_4$@Ds-AC interaction, we performed electron density differences analysis, which was provided in Fig. 7e and f. It is clearly showing regions of electron accumulation (yellow) and depletion (cyan), confirming significant charge redistribution upon hybrid formation. Electron accumulation was primarily observed around the Fe and Mo

centers, while electron depletion occurred in the carbon substrate and interfacial oxygen atoms. This indicated that the carbon support acted as an electron donor, transferring charge to the $FeMoO_4$ active sites. More importantly, the asymmetric charge distribution between the Fe and Mo atoms suggested the presence of interfacial electronic polarization, which was an indication of bimetallic electronic coupling. The charge redistribution enhanced the electronic interaction between the Fe and Mo centers, leading to the formation of electronically coupled active sites. The formation of Fe–C, Mo–C, and O–C interfacial bonds further facilitated charge delocalization across the interface, resulting in improved electron mobility. This enhanced charge transfer capability was critical for accelerating the multi-electron OER process.

# 7 Conclusion

We successfully produced a novel $FeMoO_4$@Ds-AC nanocomposite electrocatalyst by attaching iron molybdate nanostructures to a porous conductive carbon framework made from recovered date seed biomass. This well-designed hybrid structure combined the redox versatility of $FeMoO_4$ with the large surface area, good electrical conductivity and strong structure of the bio-derived carbon matrix. The catalyst that came out of this process worked very well under alkaline conditions and required only a 334 mV overpotential at 20 mA $cm^{-2}$ and a Tafel slope of 84 mV $dec^{-1}$, which showed that the reaction kinetics were good. Also, the $FeMoO_4$@Ds-AC electrode showed long-term operational stability and high durability, keeping steady current densities during long chronoamperometric tests of 24 h. These results clearly showed how to achieve both high performance and sustainability in OER catalysis, making the nanocomposite electrocatalyst an attractive alternative to systems based on noble metals. The increased activity was mostly due to the strong interactions at the interface between $FeMoO_4$ and Ds-AC. These interactions not only sped up charge transfer but also made more active sites available. The DFT results showed that the synthesized $FeMoO_4$@Ds-AC hybrid catalyst exhibited improved OER performance due to strong Fe–C and Mo–C coupling in the interfacial material. The interaction strength, orbital coupling and electron density between $FeMoO_4$ and the Ds-AC sheet were confirmed from the binding energy (−4.61 eV), orbital overlap between the Mo-3d and Fe-3d orbitals of $FeMoO_4$ and the C-2p states of Ds-AC sheet, and electron density redistribution. Our combined experimental and theoretical investigations highlighted the critical role of Fe–C and Mo–C coupling in the synthesized $FeMoO_4$@Ds-AC hybrid catalyst support for the rational design of high-efficiency electrocatalysts. Also, this study showed that agricultural waste recycling, which turns low-value biomass into high-performance electroactive materials, could be a way to connect environmental cleanup with energy conversion technologies. Overall, this work gives us a solid blueprint for making electrocatalysts for water splitting that are inexpensive, simple to scale up and good for the environment. It fits perfectly with the global push for clean energy technologies and the development of sustainable materials. It supports the goals of SDG 7 and SDG 12. So, the $FeMoO_4$@Ds-AC system looks like it could be a good next-generation anode material for practical alkaline water electrolysis and other energy storage and conversion systems.

# Author contributions

Rajini Murugesan: writing original draft, visualization, validation, methodology, data curation; Manova Santhosh Yesupatham: writing original draft, validation, investigation, data curation; Mandana Amiri: writing original draft, validation, investigation, data curation; reviewing, writing, editing; and Arthanareeswari Maruthapillai: writing original draft, supervision, resources, investigation, funding acquisition.

# Conflicts of interest

The authors declare no competing interests.

# Data availability

The data supporting this article have been included as part of the supplementary information (SI). Supplementary information: experimental procedures, structural and morphological characterization, DFT studies, electrochemical measurements, and additional supporting figures related to the OER, HER, and overall water splitting performance of the catalysts. See DOI: https://doi.org/10.1039/d6ra01930g.

# Acknowledgements

The authors acknowledge Dr S. Kamalakannan (the Center of Excellence in Materials for Advanced Technologies (CeMAT), SRM Institute of Science and Technology) for performing the DFT calculations. The authors also thank the SRM Supercomputer Centre (HPCC), SRM Institute of Science and Technology, for providing the computational facility. The authors acknowledge the support from the SRM Institute of Science and Technology, Kattankulathur-603203, Tamil Nadu, India.

# References

1 S. E. Hosseini and M. A. Wahid, *Renewable Sustainable Energy Rev.*, 2016, **57**, 850–866.
2 H. Tüysüz, *Acc. Chem. Res.*, 2024, **57**, 558–567.
3 K. Zhang and R. Zou, *Small*, 2021, **17**, 2100129.
4 N.-T. Suen, S.-F. Hung, Q. Quan, N. Zhang, Y.-J. Xu and H. M. Chen, *Chem. Soc. Rev.*, 2017, **46**, 337–365.
5 F. Wang, L. Xiao, Y. Jiang, X. Liu, X. Zhao, Q. Kong, A. Abdukayum and G. Hu, *Mater. Horiz.*, 2025, **12**(6), 1757–1795.
6 C. Pereira, D. M. Fernandes, A. F. Peixoto, M. Nunes, B. Jarrais, I. Kuźniarska-Biernacka and C. Freire, *Catalysis for a Sustainable Environment: Reactions, Processes and Applied Technologies*, 2024, pp. 247–297.
7 Q. Wen, Y. Zhao, Y. Liu, H. Li and T. Zhai, *Small*, 2022, **18**, 2104513.

8 A. Li, Y. Sun, T. Yao and H. Han, *Chem.–Eur. J.*, 2018, **24**, 18334–18355.
9 J. Yu, T. A. Le, N. Q. Tran and H. Lee, *Chem.–Eur. J.*, 2020, **26**, 6423–6436.
10 K. A. Jannath and H. A. Saputra, *Next Mater.*, 2025, **9**, 101164.
11 A. A. Jeffery, P. M. Austeria and Y.-H. Ahn, *Chem. Eng. J.*, 2025, 165885.
12 M. K. Adak, A. Rajput, D. Ghosh and B. Chakraborty, *ACS Appl. Energy Mater.*, 2022, **5**, 13645–13660.
13 J. A. Rodriguez, J. C. Hanson, S. Chaturvedi, A. Maiti and J. L. Brito, *J. Phys. Chem. B*, 2000, **104**, 8145–8152.
14 Z. Zhang, W. Li, T.-W. Ng, W. Kang, C.-S. Lee and W. Zhang, *J. Mater. Chem. A*, 2015, **3**, 20527–20534.
15 M. A. Deyab, T. Stankulov, E. Slavcheva, A. E. Awadallah, S. M. ElSaeed and E. G. Zaki, *J. Mol. Liq.*, 2020, **314**, 113693.
16 S. Vijayapradeep, R. S. Kumar, S. C. Karthikeyan, S. Ramakrishnan and D. J. Yoo, *Mater. Today Chem.*, 2024, **36**, 101934.
17 L. Guo, J. Li, Z. Lu, J. Zhang and C. He, *ChemSusChem*, 2023, **16**, e202300214.
18 R. Murugesan, M. S. Yesupatham, N. Agamendran, K. Sekar, C. S. S. Neethinathan and A. Maruthapillai, *Energy Technol.*, 2024, 2400882.
19 X. Long, J. Meng, J. Gu, L. Ling, Q. Li, N. Liu, K. Wang and Z. Li, *Chin. J. Struct. Chem.*, 2022, **41**, 2204046–2204053.
20 Z. Yang, C. Yan, M. Xiang, Y. Shi, M. Ding and J. Hui, *Int. J. Energy Res.*, 2021, **45**, 8474–8483.
21 A. Gayathri, M. Vijayarangan, M. Sangamithirai, V. Ashok, J. Jayabharathi and V. Thanikachalam, *Energy Fuels*, 2023, **37**, 19812–19821.
22 V. Selvanathan, D. K. Sarkar, M. Mottakin, M. A. Islam, H. Almohamadi, N. H. Alharthi, T. S. Kiong and M. Aktharuzzaman, *J. Taiwan Inst. Chem. Eng.*, 2023, **151**, 105131.
23 M. Bhatt, K. Gautam and A. K. Sinha, *Discover Chem.*, 2025, **2**, 1–42.
24 A. Arshad, S. Yun, Y. Si, F. Han, Y. Zhang, Y. Zhang, Z. Wang and C. Wang, *J. Power Sources*, 2020, **451**, 227731.
25 Y. Ge, Y. Yan, P. Yan, H. Mao, L. Li, X. Du, Q. Wang and H. Li, *J. Environ. Chem. Eng.*, 2025, 118298.
26 Q. Wang, R. Yu, D. Shen, Q. Liu, K. H. Luo, C. Wu and S. Gu, *Fuel*, 2023, **333**, 126368.
27 Q. Wang, Z. Fei, D. Shen, C. Cheng and P. J. Dyson, *Small*, 2024, **20**, 2309830.
28 K. N. Dinh and V. G. Gomes, *Carbon*, 2020, **157**, 515–524.
29 S. Sekar, A. T. A. Ahmed, S. M. Pawar, Y. Lee, H. Im, D. Y. Kim and S. Lee, *Appl. Surf. Sci.*, 2020, **508**, 145127.
30 Y. Gao, S. Hu, Y. Zhou and S. Zhang, *Int. J. Hydrogen Energy*, 2019, **44**, 27806–27815.
31 L. Deng, Y. Yuan, Y. Zhang, Y. Wang, Y. Chen, H. Yuan and Y. Chen, *ACS Sustain. Chem. Eng.*, 2017, **5**, 9766–9773.
32 S. Wang, H. Nam, T. B. Gebreegziabher and H. Nam, *Eng. Rep.*, 2020, **2**, e12083.
33 H. Wang, H. Xie, Q. Cao, X. Li, B. Liu, Z. Gan, H. Zhang, X. Gao and G. Zhou, *Environ. Sci. Pollut. Res.*, 2022, **29**, 35443–35458.
34 Y. Gou, Q. Liu, Z. Liu, A. M. Asiri, X. Sun and J. Hu, *Inorg. Chem. Front.*, 2018, **5**, 665–668.
35 M. Wang, Y. Cao, J. Tian, J. Xie, H. Chai and J. Ren, *Nano Res.*, 2026, **19**(3), 94908295.
36 Y. Chang, L. Kong, D. Xu, X. Lu, S. Wang, Y. Li, J. Bao, Y. Wang and Y. Liu, *Angew. Chem., Int. Ed.*, 2025, **64**, e202414234.